Materials Science & Engineering A 759 (2019) 142–153

Contents lists available at ScienceDirect

Materials Science & Engineering A

journal homepage: www.elsevier.com/locate/msea

Twin formation from a twin boundary in Mg during in-situ nanomechanical testing

Lin Jiang[a,e], M. Arul Kumar[b], Irene J. Beyerlein[c], Xin Wang[a], Dalong Zhang[a,f], Chuandong Wu[a], Chase Cooper[a], Timothy J. Rupert[a], Subhash Mahajan[d], Enrique J. Lavernia[a], Julie M. Schoenung[a,*]

[a] Department of Materials Science and Engineering, University of California, Irvine, CA, 92697, USA
[b] Materials Science and Technology Division, Los Alamos National Laboratory, Los Alamos, NM, 87545, USA
[c] Mechanical Engineering Department, Materials Department, University of California, Santa Barbara, CA, 93106, USA
[d] Department of Materials Science and Engineering, University of California, Davis, CA, 95616, USA
[e] Materials & Structural Analysis, Thermo Fisher Scientific, Hillsboro, OR, 97124, USA
[f] Pacific Northwest National Laboratory, Richland, WA 99354, USA

ARTICLE INFO

Keywords:
Grains and interfaces
Magnesium alloys
Plasticity
Modeling/simulations
Characterization

ABSTRACT

An important fundamental question regarding deformation twinning is whether it is possible for twins to nucleate at boundaries or interfaces when specific stress fields are present. A corollary that follows from this question is: if this is indeed possible, what determines the proper stress field and how does it occur at the nanoscale? Here, we demonstrate the application of an in-situ nanoindentation approach to confine and dynamically capture the stages in the formation of a deformation twin at an internal twin boundary in single crystal Mg. We observe the formation of contraction twin embryos at the pre-existing extension twin boundary, and the subsequent propagation of the twin embryos into the crystal. We reveal an intermediate step, involving the coalescence of tiny embryos into a larger embryo before the nucleus emanates into the crystal. De-twinnning of the twin embryos is captured during unloading and shown to leave a remnant nanosized twin (< 10 nm) after complete unloading. A 3D full-field, crystal plasticity model identifies that the twin type and variant selection of the stable embryo are governed by the internal local stress state prevailing at the pre-existing twin boundary. The possible role played by $< c+a >$ dislocations and boundary structure (incoherent vs. coherent) in embryo formation, as suggested by the TEM and modeling analyses, are discussed.

1. Introduction

Deformation twinning (DT) is one of the main mechanisms for plastic deformation of hexagonal close packed (HCP) metals, such as Mg, Ti, and Zr and their alloys. The rate at which DTs form and grow has a marked effect on the mechanical behavior of HCP metals [1–4]. The introduction of nanoscale DT arrays is considered to significantly enhance strength and ductility of HCP metals, which requires understanding DT mechanisms [5–7].

Over the years, extensive experimental, analytical and computational studies have been devoted to understanding twinning mechanisms [1–4]. However, the ultrafine atomic scales and ultrafast kinetics involved in the formation of a twin embryo under mechanical strain have precluded direct observation [5–7]. Current studies on DT mechanisms has mostly focused on post-mortem characterization of deformed HCP materials, using electron backscatter diffraction (EBSD) spanning submicron to micron scale twins [8–10], and high-resolution transmission electron microscopy (TEM) of twin boundaries/interfaces [11]. These studies have provided valuable and detailed information on twin structure and spatial location. Most recent insights into early twin formation provide descriptions of "serrated" twin boundaries revealing the elementary defects responsible for twin migration [11] and "paired" twins at the grain boundaries that signify strong relationships between the twin and the properties of the boundary from which it originated [10,12]. However, these and other studies cannot address and, indeed, seldom discuss the stages in the formation of twins at internal boundaries. To date, basic questions, like how twin nucleation at a boundary is accomplished, still remain.

In this study, we combine in-situ straining in the TEM and 3D full-field crystal plasticity modeling of discrete twins to understand the

---

[*] Corresponding author.
E-mail address: julie.schoenung@uci.edu (J.M. Schoenung).

https://doi.org/10.1016/j.msea.2019.04.117
Received 21 January 2019; Received in revised form 20 April 2019; Accepted 30 April 2019

stages in the nucleation of a twin embryo from an internal boundary in single crystal Mg. The approach involves application of a stress to a localized nanoscale region of a pre-existing twin boundary in a single crystal free-standing foil and observing the events that unfold in the TEM. The experimental design described in this work enables a highly localized stress concentration around the probe tip, designed to trigger nucleation of the twins. This very small stress field can confine twinning events to the nanoscale region around the pre-existing extension twin (TTW) boundary. Thus, twin growth beyond the local stress environment is not promoted. With this methodology, the nucleation of a stable twin embryo at a boundary was observed at the nanoscale, with embryo creation being preceded by dislocation glide and formation of a new boundary (on which the embryo grew). Transition to a twin lamella involved a reversible coalescence and propagation into the crystal. Accompanying multiscale, crystal plasticity calculations further predicted that the variant selected by the formation of stable embryos was governed by the local stress state, which significantly deviated from the applied macroscopic stress state.

2. Experimental

2.1. Sample preparation

A Mg single crystal of (0001) orientation (purity 99.999%) was purchased from Goodfellow (Coraopolis, PA, USA). Slices, approximately 500 μm thick, were sectioned from the single crystal using a wire saw with minimal speed and load. These slices were then mechanically polished, with a final mechanical step of 50 nm SiO_2 slurry in a diluted solution, and etched to remove the damaged surface layers and reveal the presence of any twins. Multiple H-bar type foils (20 μm in length, 10 μm in width, 150 nm in thickness), as shown in Figs. S1a–b, were prepared from the slices by using the focused ion beam (FIB) on a FEI Scios 3-D dual beam (SEM/FIB) system (Hillsboro, OR). Before the in-situ nanoindentation, some pre-existing twins were introduced in the H-bar foils due to the stress induced by the mechanical polishing. Electron back-scattered diffraction (EBSD) mapping was used to identify the extension twins in these H-bar foils. Foils with pre-existing rope-like or triangular-like shaped twins ((0–112) [01–11] V5 variant) were selected for the in-situ scanning transmission electron microscopy (STEM) local nanoindentation experiment, as described below.

2.2. In-situ STEM nanoindentation

Two in-situ experiments were performed at two selected pre-existing extension twins (TTWs): one at the boundary of a rope-like TTW and the other at the boundary of a triangular-like TTW. These in-situ nanoindentation experiments were conducted on an FEI Scios 3-D dual beam instrument equipped with both a nanoscale probe and a STEM detector located beneath the specimen. Fig. 1a and b is an image inside the SEM chamber showing the experimental set-up for the in-situ STEM local nanoindentation experiment. The nanoscale probe was used to apply a load perpendicular to the (0001) axis to favor twin formation, as schematically shown in Fig. 1c and d. The loading created a local strain/stress field in the foil as shown in Figs. S2–S3. The total displacement was approximately 250 nm, and the moving speed of the probe was controlled at a rate of 5 nm/s. Microstructural evolution at the TTW tip region was monitored by the STEM detector operated at 30 kV. After in-situ STEM nanoindentation, TEM/HRTEM micrographs of the twin tip region were acquired on JEOL JEM-2500SE and JEM-2800 microscopes operated at 200 kV.

The reason these twins were examined during in-situ loading was to promote and identify the structures of twins that could potentially form at the twin boundaries. To capture ultrafast twinning events at the nanoscale, several additional steps were taken in the design of the in-situ loading experiment. First, the STEM views were selected to allow for the possibility of revealing twin variants. Bright-field, dark-field and high angular dark-field STEM views were all utilized at the same time to capture the twinning events. The combined instrumentation and different STEM views allowed the twin embryos to be distinguished from the stress band contrasts introduced by the nanoscale probe. While in TEM viewing conditions, the twins might not be visible due to the stress band contrasts. Second, a very sharp needle with a diameter of only ~50–100 nm (Fig. 1d) was used to apply the local stress. This design allowed for the application of a highly localized stress concentration around the probe tip, designed to trigger the propagation of the TTW tip. Third, we ensured that the Mg foil was thin (approximately 150 nm thick), so the twin that formed was likely through-thickness, and therefore there was no difference between what was seen on the surface and what was happening below the surface.

Last, the deformation depth was designed on the basis of ANSYS mechanical analysis of the stress state in the Mg foil, so that the total deformation introduced by the applied local stress could be recovered after unloading (retracting of the probe). Fig. S2a shows the set-up of the nonlinear simulation (ANSYS 17.0; ANSYS, Inc., Canonsburg, PA, USA). The ANSYS model was used to design the stress and strain distributions during the in-situ nanoindentation experiments. The plasticity curves of pure Mg (Fig. S1c) were input into the simulation to include the non-elastic features in the model. The diameter (100 nm), contact angle (45°) and total displacement of the probe were the same as those in the experimental set-up. The entire Mg foil was treated as a single crystal, not including the pre-existing tensile twins in the ANSYS simulation. The equivalent plastic strain distribution near the probe tip after full loading is seen in Fig. S2d. The strain and stress distributions simulated by the ANSYS during loading and unloading are shown in Figs. S2 and S3, respectively.

From the simulations, we observe that the strain around the TTW tip reached the maximum value at peak displacement (full load) and after full unloading, the strain around the TTW tip reduced close to zero. Moreover, the stress field in the Mg foil during unloading was the reverse of the stress field during loading, as seen in Fig. S3. During loading, the stress field intensified toward the probe tip, leading to a positive tensile stress on the TTW, as shown in Figs. S3a–b. During unloading, a certain amount of strain on the foil was recovered (Fig. S2) and the stress field reversed to produce a negative compressive stress on the TTW, as shown in Figs. S3c–d. These results confirmed that the stress states generated could possibly introduce twinning during the loading and de-twinning during the unloading around a TTW tip.

2.3. Crystal Plasticity Fast-Fourier Transform simulation

To help interpret the events observed during in-situ testing, we sought to calculate the local stress fields using a Crystal Plasticity Fast-Fourier Transform (CP-FFT) model. The original FFT formulation was developed to study the local and effective mechanical response of composite materials [13,14]. This approach was later extended for polycrystalline materials to relate the effective and local constitutive responses to anisotropy and heterogeneities in microstructural properties [15–18]. This model was recently adapted to calculate the spatially resolved micromechanical fields in elastic-plastic crystals containing deformation twins [19–23]. In such calculations, the domain shape, boundary crystallography, and characteristic shear transformation strain of the twin type are taken into account. In the current study, we adopt the infinitesimal elasto-visco-plastic formulation of the CP-FFT model. Within this framework, the constitutive behavior is given by

$$\sigma(x) = C(x): \varepsilon^{e}(x) = C(x): (\varepsilon(x) - \varepsilon^{p}(x) - \varepsilon^{tr}(x)) \tag{1}$$

In the above expression, $\sigma(x)$ is the Cauchy stress tensor, $C(x)$ is the elastic stiffness tensor, $\varepsilon(x)$, $\varepsilon^{e}(x)$, and $\varepsilon^{p}(x)$ are the total, elastic and plastic strain tensors, and ε^{tr} is the transformation strain. The local stress field at a material point x is solved using an implicit time discretization of the form:

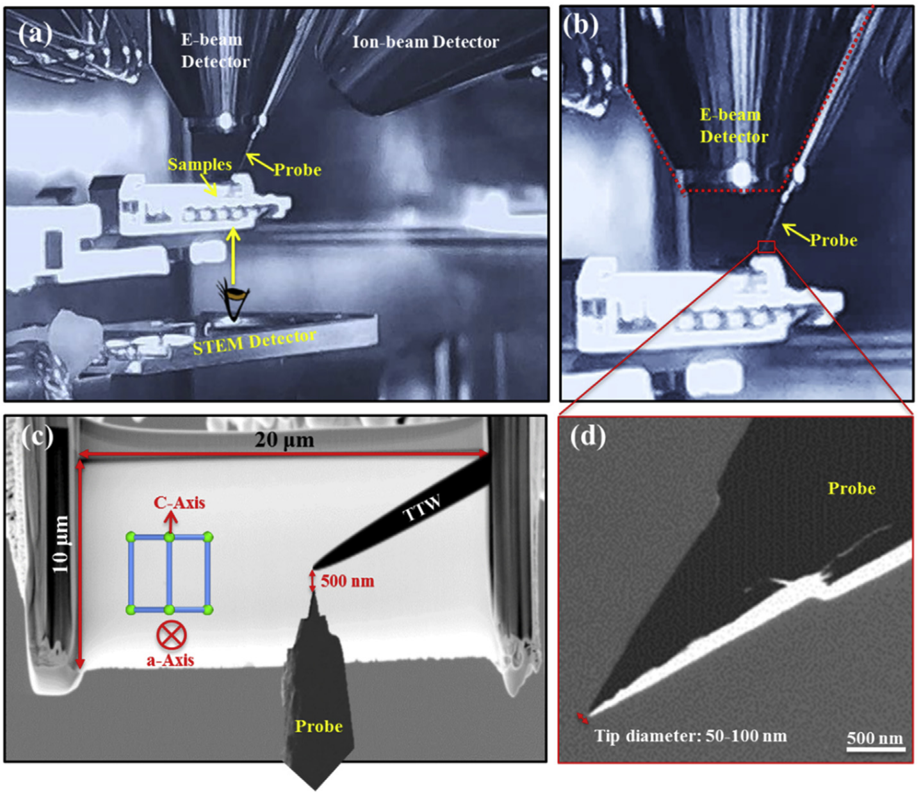

Fig. 1. Experimental set-up for the application of in-situ straining. (a–b) An image showing the in-situ strain apparatus inside the SEM/FIB chamber. (c) A schematic of a Mg thin foil with a-axis perpendicular to the surface. The location of the probe is also illustrated. (d) a SEM image to show the probe.

$$\boldsymbol{\sigma}^{t+\Delta t}(x) = \mathbf{C}(x):(\boldsymbol{\varepsilon}^{t+\Delta t}(x) - \boldsymbol{\varepsilon}^{p,t}(x) - \dot{\boldsymbol{\varepsilon}}^{\mathrm{p,t+\Delta t}}(x)\Delta t - \boldsymbol{\varepsilon}^{\mathrm{tr,\,t}}(x) - \Delta\boldsymbol{\varepsilon}^{\mathrm{tr,t+\Delta t}}(x)) \tag{2}$$

Within the twin domain, twin transformation strain is imposed. To build-up the twinning transformation, successive shear increments are imposed within the twin domain using the following strain increments:

$$\Delta\boldsymbol{\varepsilon}^{tr}(x) = \mathbf{m}^{tw}(x)\Delta\gamma^{tw}(x) \tag{3}$$

For material points outside the twin domains, $\Delta\varepsilon^{tr}(x)$ is zero. The tensor $\boldsymbol{m}^{tw} = \frac{1}{2}(\boldsymbol{b}^{tw} \otimes \boldsymbol{n}^{tw} + \boldsymbol{n}^{tw} \otimes \boldsymbol{b}^{tw})$ is the Schmid tensor associated with the twin system, where $\mathbf{b}^{\mathrm{tw}}$ and $\mathbf{n}^{\mathrm{tw}}$ are unit vectors along the twinning direction and the twin plane normal, respectively. The number of increments $\mathrm{N}^{\mathrm{twincr}}$ needed to reach the characteristic-twinning shear, s^{tw} is simply:

$$\Delta\gamma^{tw}(x) = \frac{s^{tw}}{N^{twincr}} \tag{4}$$

In the calculations, we set the time increment Δt and $\mathrm{N}^{\mathrm{twincr}}$ sufficiently low and high, respectively, to ensure convergence.

2.4. Twinning simulation

The CP-FFT model was designed to replicate the local stress distribution at or around the extension twin tip. The calculation considers a foil of single crystal Mg with its c-axis oriented in-plane and the a-axis normal to the plane of the film. The a-axis is also the loading direction for the applied local stress. This setup consists of one orientation (grain) finely discretized, which will contain the twins, surrounded by a buffer layer, see Fig. 2. The simulation unit cell is assumed to be periodic in all three directions and discretized into 3 × 750 x 750 voxels with a buffer layer 25 voxels thick, which is sufficient for making the spatially resolved stress distribution in the cell interior insensitive to how the boundary conditions are applied.

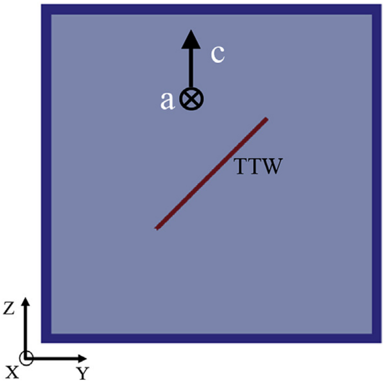

Fig. 2. Schematic representation of EVP-FFT model simulation unit cell with (0–112) [01–11] tensile twin. The unit cell is discretized into 3 × 750 x 750 voxels with a buffer layer 25 voxels thick. The grain crystal orientation is chosen in such a way that its c- and a-axes are aligned with Z and X directions, respectively.

A TTW lamella of the (0–112) [01–11] variant, the same variant as in the experiment, is inserted in the center of the model foil. Within this fine lamella twin region, we updated the lattice orientation, such that it follows the twinning-matrix 86.3° relationship, and imposed the characteristic twinning shear (S = 0.126) for TTW formation in Mg. The twin shear is imposed in 2000 (= $\mathrm{N}^{\mathrm{twincr}}$) step increments.

After introducing the TTW, similar to in the experiment, we impose compression along the a-axis. At all stages of simulation, i.e., both TTW formation and further compression, every voxel of the simulation unit cell is assumed to accommodate deformation by a combination of elastic anisotropy and crystal plasticity [20,24]. The anisotropic elastic constants of considered pure Mg are (in GPa): $\mathrm{C}_{11} = 58.58$, $\mathrm{C}_{12} = 25.02$, $\mathrm{C}_{13} = 20.79$, $\mathrm{C}_{33} = 61.11$ and $\mathrm{C}_{44} = 16.58$ GPa [25,26].

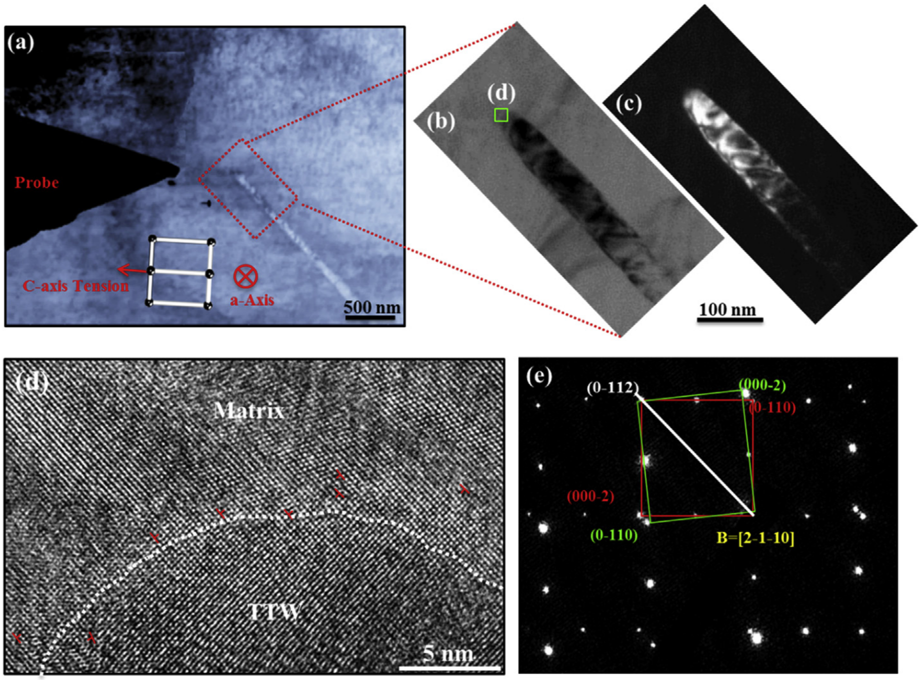

Fig. 3. The microstructure of the extension twin (TTW) with the rope-like boundary before applying the in-situ strain. (a) Bright field STEM image. (b) Bright field and (c) dark field TEM images to show the structure of the pre-existing rope-like TTW. (d) HRTEM image to show the lattice structure of the TTW tip. (e) Diffraction pattern on the rope-like TTW boundary to confirm it as a V5 TTW variant ((0–112)[01–11]).

The slip systems made available for the plastic deformation component are those belonging to the well accepted slip modes in Mg: basal < a > slip, prismatic < a > slip, and pyramidal < c + a > slip, with corresponding CRSS values: 3.3, 35.7 and 86.2 MPa, respectively [3,27].

3. Results

3.1. Microstructure of nanoscale boundaries before the in-situ nanoindentation experiment

Twins often but not always nucleate at internal microstructural boundaries or interfaces, such as grain and twin boundaries, where stress states can be concentrated [9,10,12]. In view of this fact, two particular boundaries were selected in this study. One is an incoherent boundary belonging to a rope-like {10–12} extension twin (TTW) tip, that is curved and defective, containing a non-periodic array of misfit dislocations, as shown in Fig. 3. Due its defective structure, it was chosen as a likely place to observe twin nucleation. The other boundary belongs to a triangular-like TTW (in a different sample), which was straight and mostly coherent, as shown in Fig. 4. TTWs have six twin variants, as listed in Table S1. The crystallography of the selected TTWs is (0–112) [01–11], as indicated by the selected area diffraction patterns (Figs. 3e and 4e).

3.2. In-situ real-time observation of nanoscale twinning behavior at the boundaries

During in-situ straining of the rope-like, incoherent boundary, we observed the formation of twin embryos. Fig. 5 shows the results from the in-situ bright-field STEM analysis for the sequence of events taking place at the TTW tip during the localized loading and unloading cycle. Dark-field STEM snapshots (Fig. S4) and in-situ videos (Movie S1) were also utilized to identify the twins. When the probe was first applied, the pre-existing TTW boundary propagated forward at its tip. Multiple lattice dislocations were observed to be emitted from the left side of the TTW tip and to glide into the left portion of the crystal, as shown in Fig. 5a–d. In these figures, dislocations exhibit a linear feature. The bend contours, on the other hand, exhibit ribbon-like contrast without

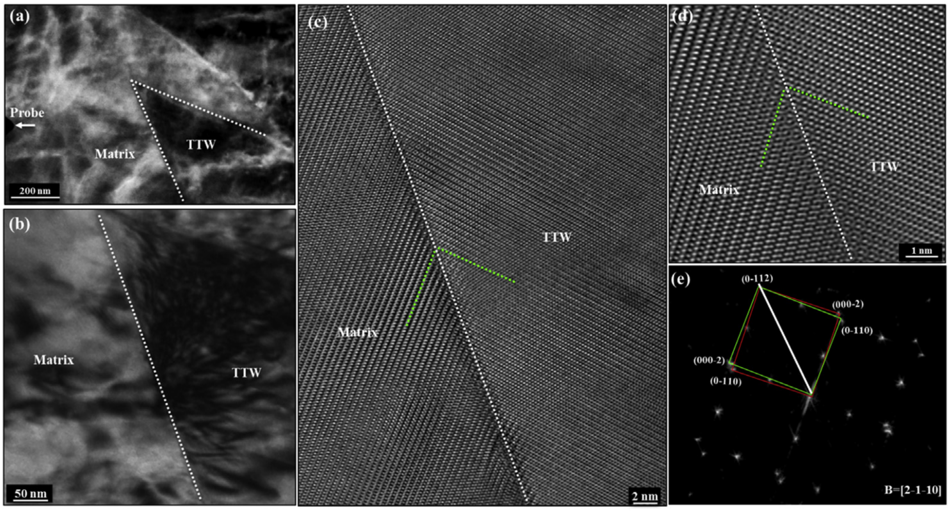

Fig. 4. The microstructure of the triangular-like extension twin (TTW) with the nearly coherent boundary before applying the in-situ strain. (a) Low magnification STEM and (b) TEM to show the morphology of the TTW boundary. (c) HRTEM and (d) fast Fourier transform (FFT) filtered HRTEM images of the TTW boundary. (e) A related FFT pattern on the boundary of TTW and matrix to identify the TTW as (0–112)[01–11] variant (V5). The dashed green lines indicate the basal planes and the dashed white lines indicate straight boundaries. (For interpretation of the references to colour in this figure legend, the reader is referred to the Web version of this article.)

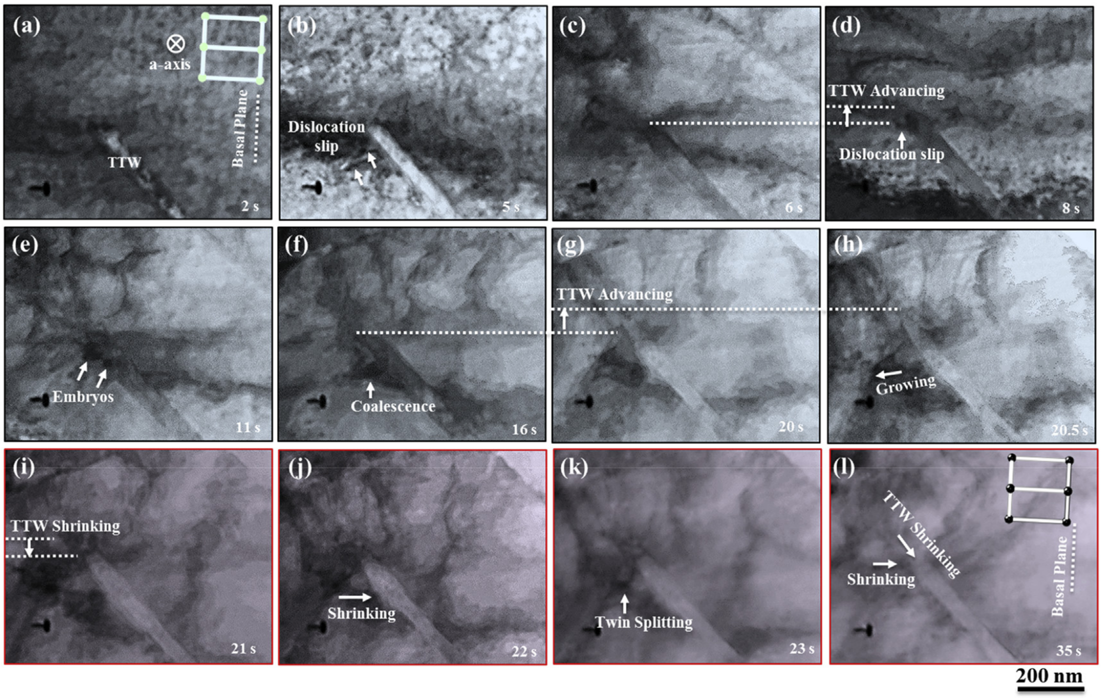

Fig. 5. Bright-field STEM snapshots to show twinning events at the boundary of the rope-like TTW during the application of in-situ strain. (a–d) Dislocation slip and TTW propagation at the initial application of the stress before the nucleation of new twin embryos. (e–h) The formation of new twin embryos, merging of the embryos and growing of the embryo during loading. (i–l) Microstructural evolution to show the shrinking and splitting of the twin during unloading. The dashed lines indicate the location of the TTW front tip. The twin embryos appear as triangle-like sharp contrasts and dislocations show linear features, whereas the stress bands exhibit as a ribbon-like contrast without a sharp interface. The twins were also identified with utilization of dark-field STEM snapshots (Fig. S4). The arrows in (b, d) indicate the locations of dislocations, appearing as straight lines. The dashed lines in (*c*-d, f-i) indicate the positions of the twin tip. The frame outlines of (i–l) indicate that the images were taken during unloading.

sharp interfaces. Shortly afterwards, in Fig. 5e, two twin embryos, each roughly 10 nm in width, were observed to nucleate at the newly produced TTW boundary on the left side of the pre-existing TTW close to its tip. The twin embryos first appear as a triangle-like sharp contrast. The abrupt change in orientation imparted by these tiny domains can be detected by combining different STEM views, which indicates that they are twins.

Supplementary data related to this article can be found at https://doi.org/10.1016/j.msea.2019.04.117.

With continued probe compression, these tiny embryos expand along the TTW boundary and coalesce into a single, larger embryo, as seen in Fig. 5f and g. Eventually, this embryo propagated into the left crystal, forming a twin lamella, as shown in Fig. 5g. With the in-situ STEM imaging, it is clear that the boundary that bounds these twin embryos is distinct from the migrating boundary of the already present TTW. Thus, these embryos belong to either new twin variants of TTW or new types of twins. While this new “parasitic” twin nucleates and emanates from the side of the TTW, the TTW tip continues to propagate forward. The results demonstrate that a critical step in the formation of a twin under stress involves the creation of a twin embryo of a certain size from the boundary, and that this step occurs prior to its transition into a lamella that protrudes into the crystal.

To examine the reversibility of these events, we reduced the applied stress by gradually retracting the probe. The unloading caused the TTW boundary propagated under loading to migrate back, or to ‘de-twin’. Only after this TTW de-twinning did the new “parasitic” twin lamella shrink in size and migrate back towards its originating boundary. As this new twin lamella moved closer to its originating boundary, it split into two smaller embryos (Fig. 5j and k), and then each one reduced even further in size. When the probe was fully removed and the stress unloaded completely, one embryo seemed to disappear entirely while the other one shrank into a very small twin embryo ~10 nm in size (Fig. 5l). Thus, under one loading cycle, the twinning process is not entirely reversible. It is also possible that this very small remnant twin domain could be the initial embryonic structure of the twin.

Fig. 6 shows the early stages of the twinning events at the boundary of the triangular-like TTW, as captured by the STEM detectors (bright-field STEM). A similar phenomenon was observed on this triangular-like TTW as had been observed for the rope-like, incoherent twin. First, multiple lattice dislocations viewed as linear features (Fig. 6a–d) were observed to move at the left side of the coherent TTW boundary. From Fig. 6a–d, two twin embryos are seen nucleating at the left side of the TTW boundary. In time, these very small embryos expanded and coalesced into a single, larger embryo, as seen in Fig. 6e–g. Then, the embryo grew towards the left side of the pre-existing boundary, and, eventually, it became a twin with a lamella shape, as shown in Fig. 6h. During the unloading (retracting of the probe), the formed twin split into two embryos (Fig. 6i–k), and then gradually shrank into a small remnant twin (Fig. 6l). This twinning phenomenon can also be viewed under different STEM detectors, as shown in Fig. S5 (dark-field) and Fig. S6 (high angular dark-field). The corresponding in-situ videos are shown in Movies S2-S4. Significantly, just as in the prior in-situ test, we observe that twin nucleation occurs by first forming twin seeds that coalescence before the twin grows and that detwinning occur by first splitting and then shrinking.

Supplementary video related to this article can be found at https://doi.org/10.1016/j.msea.2019.04.117

3.3. Microstructure of twins formed at the boundaries

Figs. 7a and 8a present TEM images of the twins residing at the rope-like and triangular-like TTW boundaries, respectively, after the local stress is applied. The twin type and its variant can be characterized via diffraction pattern or high-resolution TEM (HRTEM) by

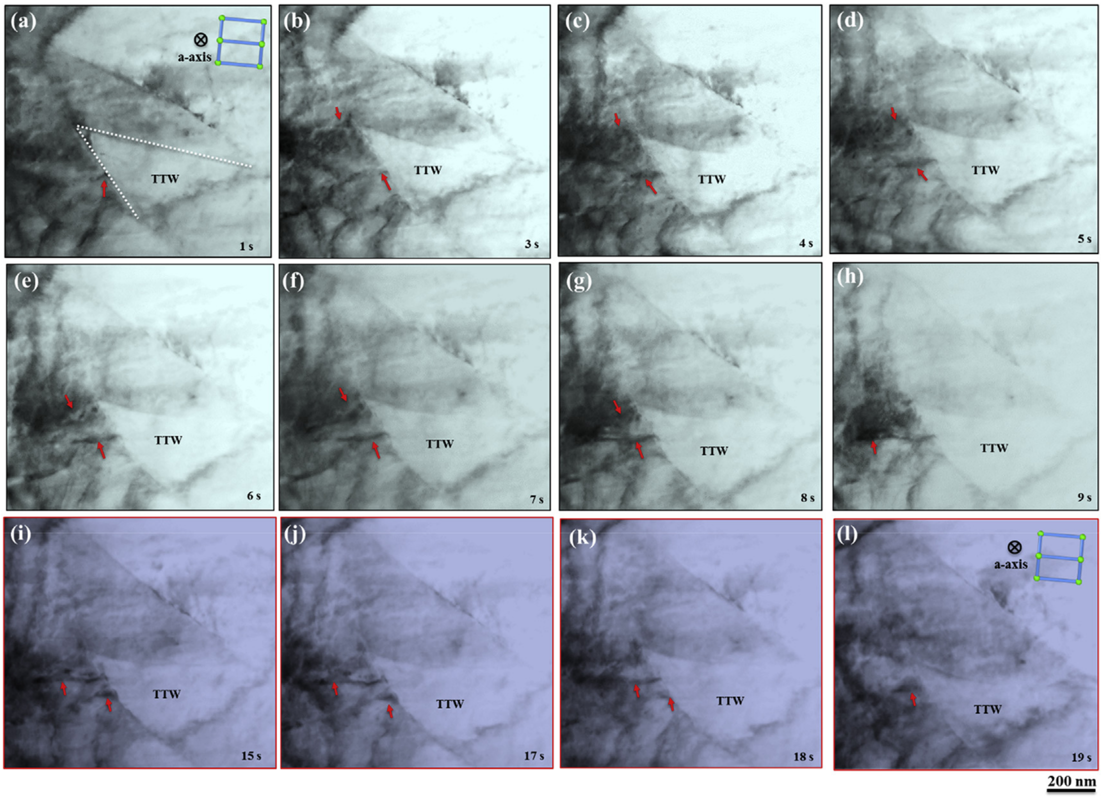

Fig. 6. Bright-field STEM snapshots to show twinning events at the boundary of the triangular-like TTW during the application of in-situ strain. (a–h) The formation of new twin embryos, merging of the embryos and growth of the embryo during loading. (i–l) Shrinkage of the twins during unloading. The solid arrows indicate the location of the twin embryos. These arrows were drawn with utilization of dark-field (Fig. S5) and high angular dark-field (Fig. S6) STEM snapshots. The frame outlines of (i–l) indicate that the images were taken during unloading.

quantifying the lattice misorientation at the twin-matrix boundary. Using both methods, we find that the misorientations at the boundaries of the twin embryos are roughly 56° (Figs. 7c and 8c), which identifies these twins as {10–11} < 10–12 > contraction twins (CTWs). CTWs are another twin type, and, unlike the TTWs, their formation is driven by the need to accommodate c-axis compression. Using Fast Fourier Transform (FFT) patterns (Fig. 7b), diffraction patterns (Fig. 8b), and HRTEM images (Fig. 7c–f and Fig. 8c–e) the crystallography of both CTWs is determined to be (0–111) [01-1-2] (denoted as V4 in Table S1).

Two features are worth noting in Figs. 7 and 8. First, before stress was applied, the boundary of the triangular-like TTW was straight and mostly coherent (Fig. 4) but after applying stress, part of the coherent TTW boundary became incoherent with curved steps, as indicated by the dashed line in Fig. 8c–e. Second, the CTW that formed at the rope-like TTW boundary is much smaller than the CTW that formed at the triangular-like TTW boundary. The CTW at the boundary of the

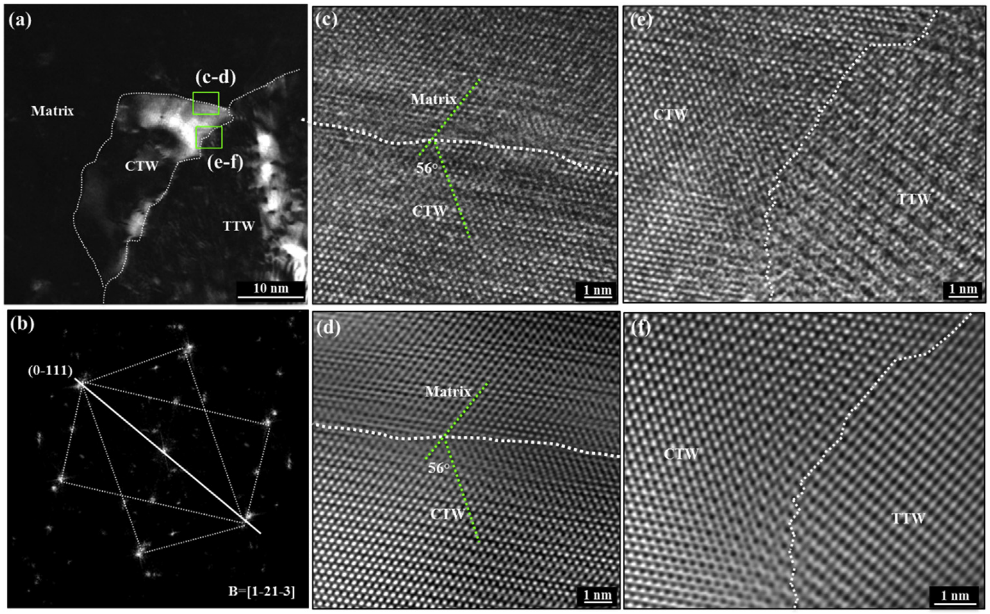

Fig. 7. The microstructure of the remnant of the de-twinned CTW at the boundary of the rope-like TTW after the in-situ test. (a) A dark field TEM to identify the CTW embryo. (b) A Fast Fourier Transform (FFT) pattern on the boundary of CTW and matrix to identify the CTW as (0–111) [01-1-2] variant (V4). (c) HRTEM and (d) FFT filtered HRTEM on the boundary of CTW and matrix. (e) A HRTEM and (f) a FFT filtered HRTEM image of the boundary between TTW and CTW. The dashed green lines indicate the basal planes and the dashed white lines indicate curved twin boundary. (For interpretation of the references to colour in this figure legend, the reader is referred to the Web version of this article.)

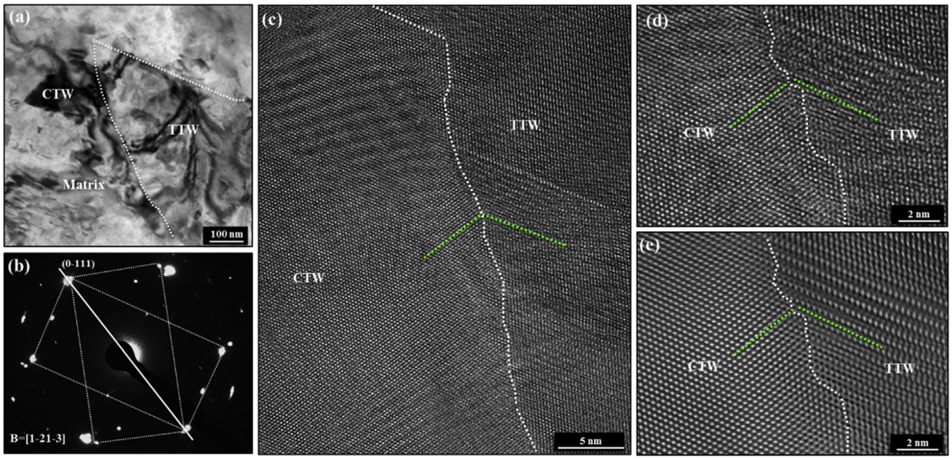

Fig. 8. The microstructure of the remnant of the de-twinned contraction twin (CTW) at the boundary of the triangular-like TTW after the in-situ test. (a) A low magnification TEM image and (b) selected area diffraction pattern to identify the CTW as (0–111) [01-1-2] variant (V4). (*c*–d) HRTEM images of the boundary between TTW and CTW and (e) related fast Fourier transform filtered HRTEM image of (d). The dashed green lines indicate the basal planes and the dashed white lines indicate curved twin boundary. (For interpretation of the references to colour in this figure legend, the reader is referred to the Web version of this article.)

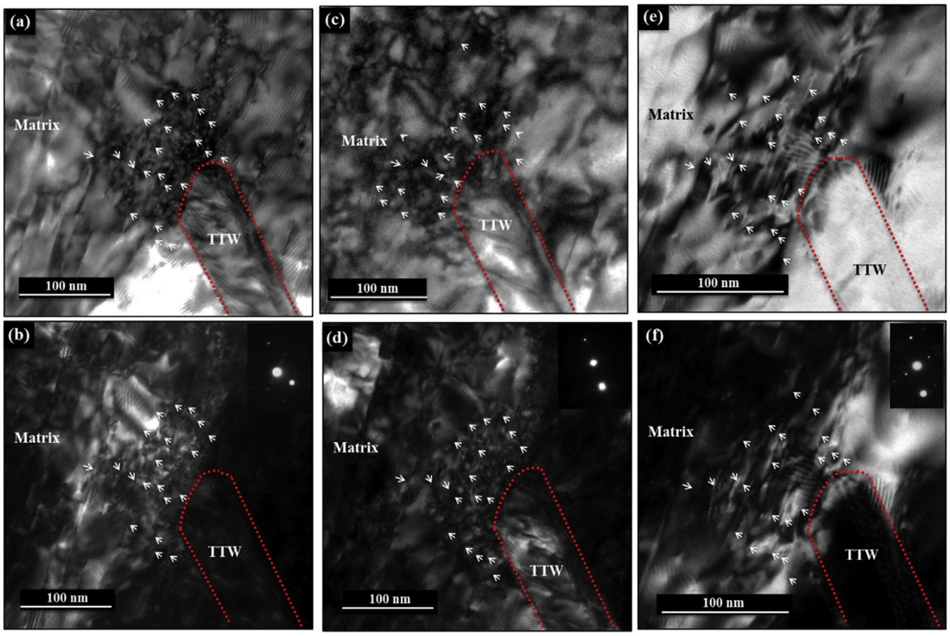

Fig. 9. Two-beam condition TEM images to show the dislocation structure around the rope-like extension twin tip. (a) Bright field TEM, and (b) dark field TEM at g = (0002) condition. Only < c > or < c + a > dislocations are visible at this two-beam TEM condition. (c) Bright field TEM, and (d) dark field TEM at g = (01–10) condition. Only < a > or < c + a > dislocations are visible at this two-beam TEM condition. (e) Bright field TEM, and (f) dark field TEM at g = (01–11) condition. All dislocations are visible at this two-beam TEM condition. The arrows indicate locations of the < c + a > dislocations. The insets of (b, d and f) are the corresponding diffraction patterns under the two-beam condition.

triangular-like TTW is approximately 100 nm wide, as seen in Fig. 8a, whereas, the TEM analysis in Fig. 7a indicates that the CTW formed at the boundary of the rope-like TTW is only ~10 nm wide.

4. Discussion

4.1. Dislocation effects on the twinning at the boundaries

While the concept of a twin embryo is not new, the stages involved in its nucleation and formation at a boundary have not been observed before. A number of post-mortem TEM studies of already deformed metals have reported twin embryos of nanometer dimension within crystals and near boundaries [28–30]. Development of a {10–12} TTW embryo from the stress-induced dissociation of large defects in a crystal has been simulated in molecular dynamics (MD) [31]. A mechanism for {10–12} extension twin embryo formation at boundaries in HCP crystals was presented and incorporated into a probability model for twin nucleation in polycrystalline Zr and Mg [32–34]. In addition, the formation of a broad, several nm wide “boundary embryo” of a {10–12} twin was simulated via MD by impinging a basal dislocation pile up on a low angle tilt boundary [35,36]. The interaction between the basal dislocations and the tilt boundary first caused a sequence of dissociations of the grain boundary dislocations, followed by the formation of many twin small embryos as the products of the dissociation reactions, and finally the coalescence of these smaller embryos into a larger one. This mechanism of “embryo incubation” within a grain boundary, however, has not been seen experimentally for any HCP twin, even the most common {10–12} twin.

It has been proposed that partial twinning dislocations (TDs), the elementary defect of a twin, can form as a product of a stress-driven reaction of dislocations [37–43]. An important implication of these models is that plasticity precedes twinning; that is, twins form from TDs, which in turn form as a result of lattice dislocations. This proposition of a transition from slip to twinning has not been well supported to date by direct experimental observation in HCP metals [44,45]. Here, at the nanoscale, the present investigation indicates that both TTW extension at the tip and plastic deformation through dislocation movement occurred prior to formation of the CTW.

To determine the nature of the local dislocation activity, the defect structures at the tip of the rope-like TTW before, during and after in-situ testing were investigated in more detail. Before loading, the tip of the rope-like TTW was curved and defective (see Fig. 3d), and there was no dislocation pile-up along the left side of the TTW tip (Fig. 3a–c). In the early stages of in-situ compression, lattice dislocation slip was active around this TTW tip, as shown in the snapshots (Fig. 5b–d and Movie S1). After in-situ testing, dislocation networks (dislocation

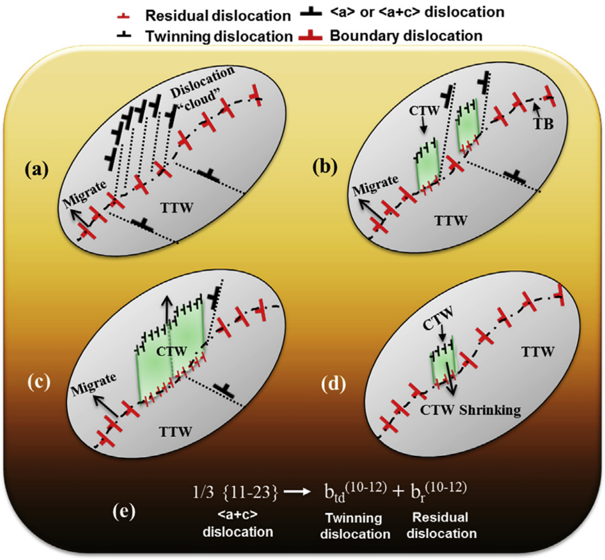

Fig. 10. Schematic to show the nucleation, growth and shrinkage of the CTW at the TTW boundary. (a) The slip dislocations pile up ahead of the TTW tip at the CTW embryo site. (b) The formation of CTW embryos, (c) the coalescence and growth of CTW embryos, and (d) the shrinkage of the CTW embryos. (e) The dislocation dissociation reaction at the TTW boundary.

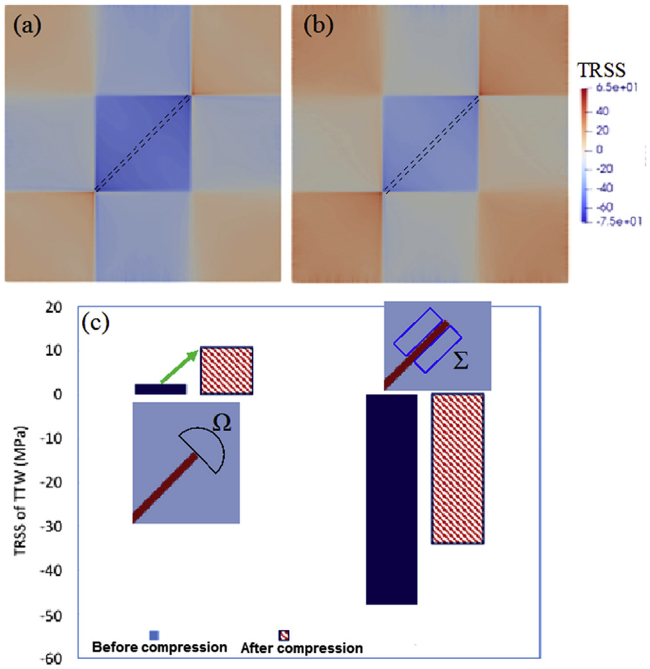

Fig. 11. The twin-plane resolved shear stress (TRSS) distribution for the simulated TTW variant: (a) before and (b) after applying compression along the a-axis. (c) The local average TRSS at the twin tip and twin side before and after a-axis compression.

entanglement and pile-up) were observed to accumulate at the left side of the TTW tip (Fig. 9), as a result of the stress concentration introduced by the nanoprobe. This dislocation entanglement can act as an obstacle to dislocation pile-up. Thus, the in-situ evidence supports the argument that lattice dislocation slip occurred at the TTW tip. The dislocation networks were further characterized in detail using multiple two-beam conditions in the TEM, as shown in Fig. 9. A high density of dislocations is visible for all three two-beam TEM conditions, indicating they have both < c > and < a > components. Thus, the dislocations in the pile-up were determined to be mostly < c + a > dislocations with a Burgers vector 1/3{11–23}.

The TTW boundaries, where high stresses and heterogeneities are located, are preferred sites for twin nucleation. At the growing TTW boundary, the gliding pyramidal < c + a > slip could have reacted to produce the TDs for the CTW [46]. Thus, twin nucleation was likely triggered when the dislocation pile-up intersects the growing TTW boundary containing an array of boundary dislocations, as schematically shown in Fig. 10a–d. As the dislocations impinge on the TTW boundary, several dislocations dissociate, forming small embryos at the TTW boundary. In the context of twinning, a dissociation reaction converts a dislocation into a product of two or more partial dislocations. Fig. 10e illustrates a boundary dissociation reaction in which partial dislocations of different types are formed. A partial dislocation, b_{td}, a type of twinning dislocation (TD), can be produced on the CTW twin plane through the reaction. Also, a residual partial dislocation, b_r. can remain on the TTW boundary after the reaction. It is noted that these TDs have a very small Burgers vector and thus are hard to be identified experimentally. The curved TTW boundary after applying the local stress, as seen in Figs. 7 and 8, can be considered to contain these partial twinning dislocations. Atomic simulation indicates that migration of a twin boundary via twinning dislocations that are dissociated from the incoming dislocations generally resulted in the curved twin boundary [47]. Specifically, after the application of the local stress, the coherent TTW boundary (Fig. 4) became incoherent, as seen in Fig. 8. This supports the concept of dissociation of the impinging lattice dislocations onto the TTW boundary.

The sequential gliding of the TDs on the twinning plane can lead to the formation of the twin embryos [46]. However, one < c + a > lattice dislocation or a few < a > dislocations generally can only dissociate into a small number of TDs [31,48]. Thus, many dislocations would need to dissociate in order to build the ~10 nm CTW embryo that was seen to eventually propagate into the crystal. Here, the in-situ observation of CTW formation suggests an intermediate stage occurring between the dissociation reaction of a lattice dislocation and the formation of a stable embryo. Unlike twins in simpler cubic materials, this {10–11} CTW lamella did not form by sequential glide of twinning partials from the originating boundary into the crystal, but by small nuclei that coalesced into larger nuclei on the boundary. The coalescence process was reported to be accomplished via pure atomic shuffling, not by the gliding of the TDs at the twin boundary [42]. We also observed a coalescence process that would suggest that under the current stress conditions, each seed nucleus was not of sufficient size to propagate forward into the crystal to form a stable lamella.

4.2. Local stress effects on the twinning at the boundaries

In this section, we use the CP-FFT model, described in Sections 2.3 and 2.4, to determine the evolution of the stress fields in the entire foil, including those locally inside and around the twin, with increasing a-axis compression.

We first analyze the driving forces that are relevant to extending the TTW by propagating the TTW boundary at the pre-existing TTW tip under a-axis probe compression. Fig. 11a and Table S2 show the twin-plane resolved shear stress (TRSS) field corresponding to the TTW, an appropriate driving force for tensile twin formation [27,32,34], without a-axis compression. As shown, the TTW-TRSS field is heterogeneous, developing particularly high positive (red) and negative TRSS (blue) values at the twin tip and sides, respectively [49–51]. Fig. 11b presents the TTW-TRSS distribution after 1% a-axis compression. Overall, the TRSS increases for all voxels, which is expected for a-axis compression. However, the increase in positive TRSS at the twin tip is more significant compared to the other regions bounding the twin. To discuss this more quantitatively, the local average TRSS at the twin front in region Ω and at the lateral sides in region Σ are calculated and shown in Fig. 11c. The results clearly show that the TRSS value at both the TTW front and lateral sides increases. Thus, a-axis compression loading

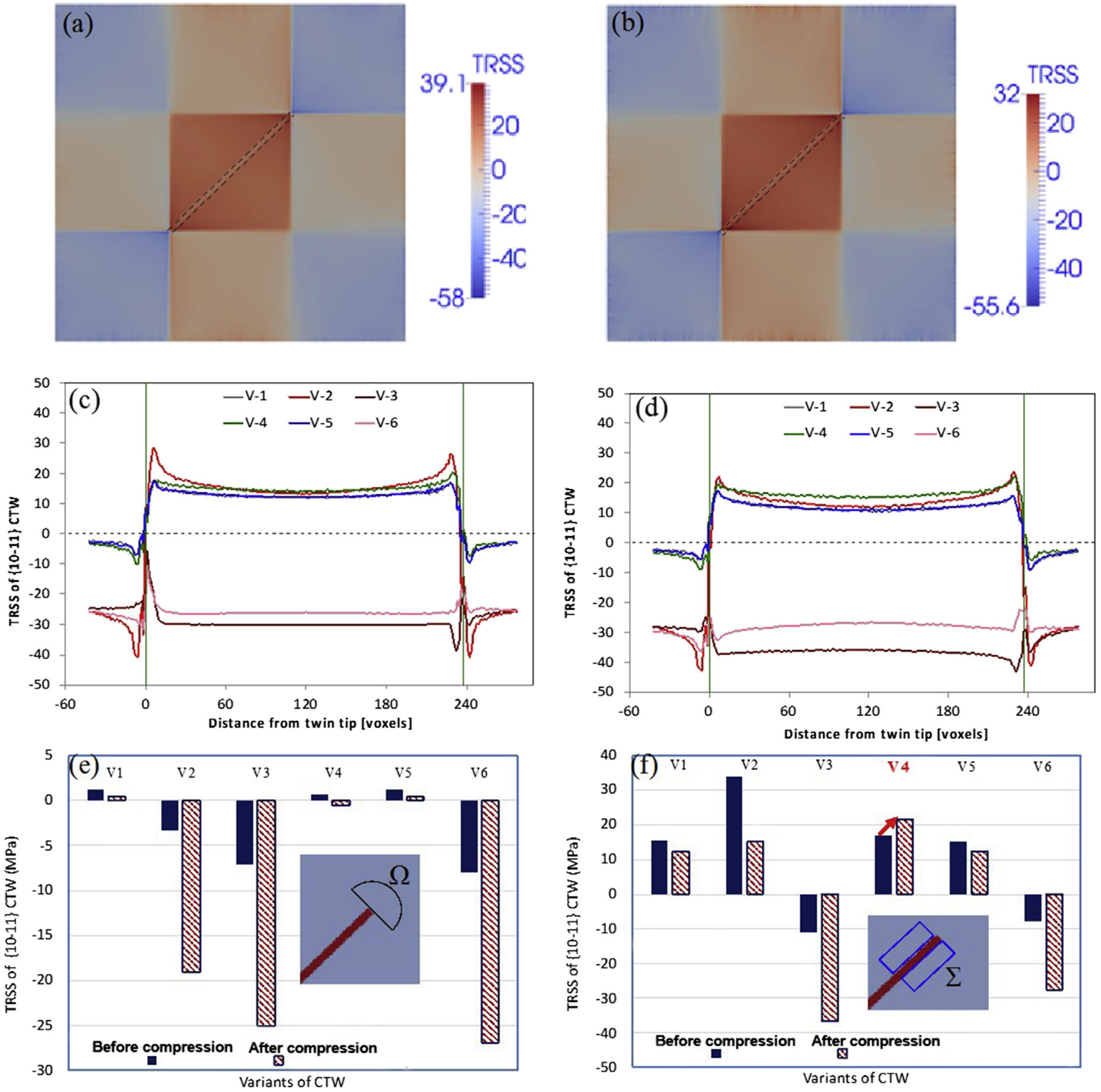

Fig. 12. The twin-plane resolved shear stress (TRSS) distribution. The TRSS distribution for variant V4 of the CTW as a result of the pre-existing TTW (a), and after applying compression along the a-axis (b). The profile of the TRSS for all six CTW variants (V1 to V6) along the TTW-matrix interface prior (c) and after (d) a-axis compression. The TRSS for a given CTW variant V1–V6 averaged within: (e) region Ω, and (f) region Σ, before and after further < a > -axis compression. Region Ω is a small (5 voxel wide) region lying in the matrix grain at the twin tip. Region Σ lies along the twin-matrix interface close to the twin tip and spans 5 voxels on both sides of the twin.

favors twin tip advancement (twin propagation) and lateral widening (twin growth). The increase in TRSS at the twin front is more significant, suggesting that the first event seen would be propagation of the twin tip.

These numerical predictions support the experimentally observed TTW propagation under a-axis probe compression. For the rope-like TTW, the initial loading drove the propagation of the TTW tip, but not lateral thickening. For the triangular-like TTW, it was clear from comparing the initial and final configurations that the twin extended in the vicinity of its tip, but the propagation of the tip could not be distinguished from lateral thickening in the in-situ test.

Next, we study the nucleation of CTW at the TTW boundaries. Interestingly, the Schmid factor on V4 under a-axis compression is zero. The question then becomes how the CTW twin type and variant observed in the experiment are selected. Were they determined by the characteristics of the dislocations that reacted to produce the embryo or by the local stress state that drove the reaction, or both? It has been noted in many postmortem metallographic studies of twin lamellae in deformed specimens that selection of the twin type (i.e., TTW or CTW) and variant of the twin (among six distinct ones for a given type) do not follow Schmid's law [52–55]. The stable CTW embryo of the V4 variant seen to nucleate here under the probe compression is yet another example of a so-called “non-Schmid twin”. Its presence and variant have no clear relationship to the externally applied load.

The likely explanation is that the selection of CTW and the particular V4 variant have to do with the local stress fields induced around the twin. Fig. 12a and b shows the twin-plane resolved shear stress (TRSS) on the CTW twin plane and in the twinning direction for the (0–111) [01-1-2] variant (denoted as V4 in Table S1). The calculated results indicate that the CTW-TRSS stress field is inhomogeneous around the TTW. The CTW-TRSS field at the tip and the sides are of opposite sign; the negative TRSS (blue) at the tip corresponds to a TRSS

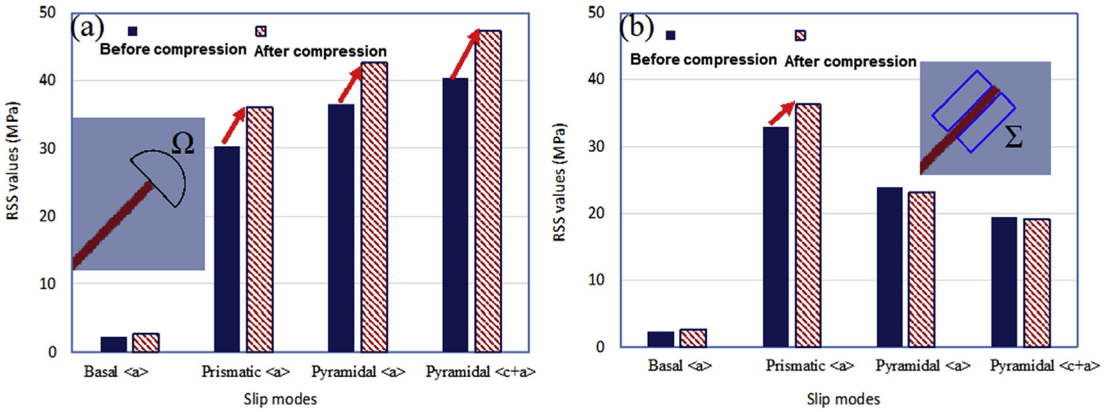

Fig. 13. The average resolved shear stress (RSS) of all four dislocation slip modes calculated in: (a) region Ω, and (b) region Σ, before and after further a-axis compression. Region Ω is a small (5 voxel wide) region lying in the matrix grain at the twin tip. Region Σ lies along the twin-matrix interface close to the twin tip and spans 5 voxels on both sides of the twin.

directed in the *anti*-CTW-twinning direction and hence would hinder V4 CTW formation. The positive values of TRSS (red) favor the CTW formation on the sides of the TTW. Even without application of the load, the calculated TRSS stress fields explain the formation of the CTW on the sides of the TTW, which is consistent with the response observed in the in-situ experiments. Fig. 12b shows the CTW-TRSS distribution for V4 under a-axis compression. The loading does not alter the stress distribution significantly.

To understand why V4 was selected, all possible CTW variants must be considered. In Fig. 12c and d, the TRSS of all CTW variants along TTW interface before and after the a-axis compression are shown, respectively. The analysis identifies variants V1, V2, V4 and V5 with positive CTW-TRSS at the TTW lateral sides close to the twin tip and the other two V3 and V6 with negative CTW-TRSS values. Thus, among the four former variants, any one or multiple variants can nucleate. Fig. 12d presents the CTW-TRSS after a-axis compression. Notably, only V4 increases the TRSS locally at the TTW tip, while other variants decrease its CTW-TRSS. The rise of V4 only under a-axis compression provides some explanation for the selection of this variant during the in-situ experiment.

This notion can be pursued more quantitatively by calculating the twin resolved shear stresses for all six variants of the CTW locally around the TTW twin boundary, both at the tip Ω and lateral Σ regions (see inserts in Fig. 12). As seen in Fig. 12e and f, the model predicts that, under no applied loading, the TTW-induced stress field favors only some of the CTW variants on the lateral sides Σ of the twin (V1, V2, V4, V5), but none of them in the front region Ω. The applied load is then increased, and it is found that the resolved shear stress on only the V4 CTW variant, as seen experimentally, increases, while the rest decrease. This result suggests that the dynamics of TTW extension at the tip and subsequent CTW growth on the lateral side seen in the in-situ experiment is a consequence of the character of the local stress field along the TTW boundary, which results from accommodating the shear and reorientation of the TTW twin domain.

In addition to the twin resolved local stress fields, the types of dislocations activated in the vicinity of the twin tip are also important, as they are the most likely to interact with the twin boundary. To study slip activity, the resolved shear stress on each of the slip modes is calculated and averaged for the region in front of the TTW tip (region Ω) and immediate lateral sides of the twin tip (region Σ), where the CTW embryos were nucleated. Fig. 13a and b shows that loading increases the activity of prismatic $< a >$ slip and pyramidal $< c+a >$ slip at the twin front and at the lateral regions. It is also predicted that the relative amounts of pyramidal $< c+a >$ slip were highest in the Ω region, while those for prismatic $< a >$ slip were highest in the lateral Σ region. These results are in qualitative agreement with the observation of slip dislocations during loading and tangles of $< c+a >$ dislocations after the local stress is applied around the TTW tip.

It is noteworthy that after applying the local stress along the a-axis to a certain level, we then started to release the load. Due to this process, the propagated TTW started to de-twin and, in time, the newly formed CTW also started to de-twin. The FFT based calculation provided above for the loading state can be extended for the unloading state. The de-twinning of the TTW creates the local stress state in the opposite sense, and then it leads to the de-twinning of the CTW. So, the twinning and de-twinning of CTW is not directly related to the external load applied by the probe, but rather modifies the local stresses induced by the TTW and leads to the twinning and de-twinning of the CTW.

Lastly, we compared the twinning phenomenon at the two different pre-existing TTWs: a rope-like TTW (Figs. 5 and 7) and a triangular-like TTW (Figs. 6 and 8). Although, they have different shapes, they both exhibited a similar sequence of twinning events: TTW propagation, CTW nucleation, coalescence. The CTW variant that nucleated at the TTW boundary was also the same, indicating the stress-fields introduced by these two TTW boundaries are similar. The noteworthy differences are that the size of the CTW nucleated at the triangular-like TTW was much larger than the one at the rope-like TTW. This difference suggests that the favorable local stress field for CTW nucleation created by the triangular-like TTW is significantly larger compared to that created by the rope-like TTW. Since the external loading conditions on these two TTWs are the same, the difference in the critical stress for nucleation could suggest an interesting shape and size effect of the pre-existing TTWs on the intensity of the stress field prevailing at their boundaries.

5. Conclusions

In summary, we utilize in-situ straining in the TEM and 3D full-field crystal plasticity modeling to investigate the formation of nanoscale twin nuclei at boundaries in an Mg single crystal. The crystals contain a pre-existing extension {10–12} twin, in one case with a rough defective boundary and in another case a nearly coherent twin boundary. Upon loading, multiple, tiny contraction {10–11} twin embryos formed at both types of boundaries and eventually grew into the crystal as a single twin. Upon unloading, the twin detwinned, collapsing back into multiple seeds before disappearing. These findings revealed an intermediate stage in twin development involving the nucleation and coalescence of several smaller embryos along the boundary, taking place before the twin nucleus emanated from the boundary into the perfect crystal as a propagating lamella. The more defective boundary initially produced more twin nuclei, but they coalesced into a smaller single twin embryo than the CTW twin at the coherent twin boundary. After full unloading a remnant embryo a few nanometers wide still remained at both boundary types. Calculations from a multiscale CP-FFT model suggest that the formation of the CTW embryo and the selection of its particular variant were driven by the local stresses generated at the twin boundary by the twin shear and the applied external load. The methodology and findings presented here can help overcome some of the challenges in observing twin nucleation events and provide answers to important fundamental questions regarding how nanoscale twin formation at boundaries or interfaces is accomplished.

Acknowledgements

The authors acknowledge financial support from the National Science Foundation (NSF CMMI-1631873, NSF CMMI-1729829, NSF CMMI-1729887, and NSF CMMI-1723539). We also acknowledge funding from the ONR–Defense University Research Instrumentation Program under grant N00014-13-1-0668, which supported the purchase of the dual-beam FIB/SEM. MAK acknowledges OBES grant FWP-06SCPE401 for financial support. Authors are grateful to Dr. R. A. Lebensohn for making available the EVP-FFT code used here for the simulations.

Appendix A. Supplementary data

Supplementary data to this article can be found online at https://doi.org/10.1016/j.msea.2019.04.117.

References

[1] Q. Yu, Z.W. Shan, J. Li, X.X. Huang, L. Xiao, J. Sun, E. Ma, Strong crystal size effect on deformation twinning, Nature 463 (7279) (2010) 335–338.
[2] Q. Yu, L. Qi, R.K. Mishra, J. Li, A.M. Minor, Reducing deformation anisotropy to achieve ultrahigh strength and ductility in Mg at the nanoscale, Proc. Natl. Acad. Sci. Unit. States Am. 110 (33) (2013) 13289–13293.
[3] I.J. Beyerlein, X. Zhang, A. Misra, Growth twins and deformation twins in metals, Ann. Rev. Mater. Res. 44 (1) (2014) 329–363.
[4] B.Y. Liu, J. Wang, B. Li, L. Lu, X.Y. Zhang, Z.W. Shan, J. Li, C.L. Jia, J. Sun, E. Ma, Twinning-like lattice reorientation without a crystallographic twinning plane, Nat. Commun. 5 (2014) 3297.
[5] Q. Yu, M. Legros, A.M. Minor, In situ TEM nanomechanics, MRS Bull 40 (01) (2015) 62–70.
[6] Q. Yu, L. Qi, K. Chen, R.K. Mishra, J. Li, A.M. Minor, The nanostructured origin of deformation twinning, Nano Lett. 12 (2) (2012) 887–892.
[7] Y. Qian, R.K. Mishra, A.M. Minor, The effect of size on the deformation twinning behavior in hexagonal close-packed Ti and Mg, JOM 64 (10) (2012) 1235–1240.
[8] P. Molnár, A. Jäger, P. Lejček, Twin nucleation at grain boundaries in Mg–3 wt.% Al–1 wt.% Zn alloy processed by equal channel angular pressing, Scripta Mater 67 (5) (2012) 467–470.
[9] D. Shi, T. Liu, T. Wang, D. Hou, S. Zhao, S. Hussain, {10–12} Twins across twin boundaries traced by in situ EBSD, J. Alloy. Comp. 690 (2017) 699–706.
[10] H. Yu, Y. Xin, A. Chapuis, X. Huang, R. Xin, Q. Liu, The different effects of twin boundary and grain boundary on reducing tension-compression yield asymmetry of Mg alloys, Sci. Rep. 6 (2016) 29283.
[11] Y. Liu, N. Li, S. Shao, M. Gong, J. Wang, R.J. McCabe, Y. Jiang, C.N. Tomé, Characterizing the boundary lateral to the shear direction of deformation twins in magnesium, Nat. Commun. 7 (2016) 11577.
[12] L. Wang, P. Eisenlohr, Y. Yang, T.R. Bieler, M.A. Crimp, Nucleation of paired twins at grain boundaries in titanium, Scripta Mater 63 (8) (2010) 827–830.
[13] J. Michel, H. Moulinec, P. Suquet, A computational method based on augmented Lagrangians and fast Fourier Transforms for composites with high contrast, Cmes-Comput. Model. Eng. Sci. 1 (2) (2000) 79–88.
[14] H. Moulinec, P. Suquet, A fast numerical method for computing the linear and nonlinear mechanical properties of composites, Comptes Rendus De L Academie Des Sciences Serie Ii 318 (11) (1994) 1417–1423.
[15] R.A. Lebensohn, N-site modeling of a 3D viscoplastic polycrystal using Fast Fourier Transform, Acta Mater 49 (14) (2001) 2723–2737.
[16] R.A. Lebensohn, R. Brenner, O. Castelnau, A.D. Rollett, Orientation image-based micromechanical modelling of subgrain texture evolution in polycrystalline copper, Acta Mater 56 (15) (2008) 3914–3926.
[17] A.K. Kanjarla, R.A. Lebensohn, L. Balogh, C.N. Tome, Study of internal lattice strain distributions in stainless steel using a full-field elasto-viscoplastic formulation based on fast Fourier transforms, Acta Mater 60 (6-7) (2012) 3094–3106.
[18] R.A. Lebensohn, A.K. Kanjarla, P. Eisenlohr, An elasto-viscoplastic formulation based on fast Fourier transforms for the prediction of micromechanical fields in polycrystalline materials, Int. J. Plast. 32-33 (2012) 59–69.
[19] I.J. Beyerlein, M. Arul Kumar, The Stochastic Nature of Deformation Twinning: Application to HCP Materials, in: W. Andreoni, S. Yip (Eds.), Handbook of Materials Modeling & Methods: Theory and Modeling, Springer International Publishing, Cham, 2018, pp. 1–39.
[20] M. Arul Kumar, I.J. Beyerlein, C.N. Tomé, Effect of local stress fields on twin characteristics in HCP metals, Acta Mater 116 (2016) 143–154.
[21] M.A. Kumar, I.J. Beyerlein, R.A. Lebensohn, C.N. Tome, Modeling the effect of neighboring grains on twin growth in HCP polycrystals, Model Simul Mater Sc 25 (6) (2017) 064007.
[22] M.A. Kumar, I.J. Beyerlein, R.J. McCabe, C.N. Tome, Grain neighbour effects on twin transmission in hexagonal close-packed materials, Nat Commun 7 (2016) 13826.
[23] M.A. Kumar, I.J. Beyerlein, C.N. Tome, Grain size constraints on twin expansion in hexagonal close packed crystals, J Appl. Phys. 120 (15) (2016).
[24] M. Arul Kumar, A.K. Kanjarla, S.R. Niezgoda, R.A. Lebensohn, C.N. Tomé, Numerical study of the stress state of a deformation twin in magnesium, Acta Mater 84 (2015) 349–358.
[25] R.F.S. Hearmon, The Elastic Constants of Anisotropic Materials, Rev. Mod. Phys. 18 (3) (1946) 409–440.
[26] G. Simmons, H. Wang, Single crystal elastic constants and calculated aggregate properties: A Handbook, MIT press, 1971.
[27] I.J. Beyerlein, R.J. McCabe, C.N. Tome, Effect of microstructure on the nucleation of deformation twins in polycrystalline high-purity magnesium: A multi-scale modeling study, J. Mech. Phys. Solids 59 (5) (2011) 988–1003.
[28] T. Braisaz, P. Ruterana, G. Nouet, R.C. Pond, Investigation of {1012} twins in Zn using high-resolution electron microscopy: Interfacial defects and interactions, Philos. Mag. A 75 (4) (1997) 1075–1095.
[29] S.G. Song, G.T. Gray, Structural interpretation of the nucleation and growth of deformation twins in Zr and Ti-I. Application of the coincidence site lattice (CSL) theory to twinning problems in h.c.p. structures, Acta Metall. Mater. 43 (6) (1995) 2325–2337.
[30] S. Lay, G. Nouet, Morphology of (01·2) twins in zinc and related interfacial defects, Philos. Mag. A 72 (3) (1995) 603–617.
[31] J. Wang, R.G. Hoagland, J.P. Hirth, L. Capolungo, I.J. Beyerlein, C.N. Tomé, Nucleation of a twin in hexagonal close-packed crystals, Scr. Mater. 61 (9) (2009) 903–906.
[32] I.J. Beyerlein, C.N. Tomé, A probabilistic twin nucleation model for HCP polycrystalline metals, Proc. R. Soc A: Math. Phys. Eng. Sci. 466 (2121) (2010) 2517–2544.
[33] I.J. Beyerlein, R.J. McCabe, C.N. Tomé, Effect of microstructure on the nucleation of deformation twins in polycrystalline high-purity magnesium: A multi-scale modeling study, J. Mech. Phys. Solids 59 (5) (2011) 988–1003.
[34] S.R. Niezgoda, A.K. Kanjarla, I.J. Beyerlein, C.N. Tomé, Stochastic modeling of twin nucleation in polycrystals: An application in hexagonal close-packed metals, Int. J. Plast. 56 (2014) 119–138.
[35] J. Wang, S.K. Yadav, J.P. Hirth, C.N. Tomé, I.J. Beyerlein, Pure-shuffle nucleation of deformation twins in hexagonal-close-packed metals, Mater. Res. Lett. 1 (3) (2013) 126–132.
[36] J. Wang, Q. Yu, Y. Jiang, I.J. Beyerlein, Twinning-associated boundaries in hexagonal close-packed metals, JOM 66 (1) (2014) 95–101.
[37] S. Lay, G. Nouet, Interaction of slip dislocations with the (01-12) twin interface in zinc, Philos. Mag. 70 (1994) 1027–1044.
[38] R.C. Pond, A. Serra, D.J. Bacon, Dislocations in interfaces in the hcp metals - II. Mechanisms of defect mobility under stress, Acta Mater 47 (1999) 1441–1453.
[39] A. Serra, D.J. Bacon, Computer simulation of screw dislocation interactions with twin boundaries in H.C.P. metals, Acta Metall. Mater. 43 (1995) 4465–4481.
[40] A. Serra, D.J. Bacon, A new model for {10-12} twin growth in hcp metals, Philos. Mag. 73 (1996) 333–343.
[41] A. Serra, D.J. Bacon, R.C. Pond, Dislocations in interfaces in the hcp metals - I. Defects formed by absorption of crystal dislocations, Acta Mater 47 (1999) 1425–1439.
[42] J. Wang, I.J. Beyerlein, J.P. Hirth, Nucleation of elementary and twinning dislocations at a twin boundary in hexagonal close packed crystals, Modell. Simul. Mater. Sci. Eng. 20 (2012) 024001.
[43] M.H. Yoo, J.K. Lee, Deformation twinning in h.c.p. metals and alloys, Philos. Mag. 63 (1991) 987–1000.
[44] I.J. Beyerlein, C.N. Tomé, A dislocation-based constitutive law for pure Zr including temperature effects, Int. J. Plast. 24 (5) (2008) 867–895.
[45] M.H. Yoo, J.K. Lee, Deformation twinning in h.c.p. metals and alloys, Philos. Mag. A 63 (5) (1991) 987–1000.
[46] L. Capolungo, I.J. Beyerlein, Nucleation and stability of twins in hcp metals, Phys. Rev. B 78 (2) (2008) 024117.
[47] J. Wang, I.J. Beyerlein, C.N. Tomé, Reactions of lattice dislocations with grain boundaries in Mg: Implications on the micro scale from atomic-scale calculations, Int. J. Plast. 56 (2014) 156–172.
[48] J. Wang, J.P. Hirth, C.N. Tomé, (-1012) Twinning nucleation mechanisms in hexagonal-close-packed crystals, Acta Mater 57 (18) (2009) 5521–5530.
[49] M.A. Kumar, I.J. Beyerlein, C.N. Tome, Effect of local stress fields on twin characteristics in HCP metals, Acta Mater 116 (2016) 143–154.
[50] M.A. Kumar, B. Clausen, L. Capolungo, R.J. McCabe, W. Liu, J.Z. Tischler, C.N. Tome, Deformation twinning and grain partitioning in a hexagonal close-packed magnesium alloy, Nat Commun 9 (2018) 4761.
[51] M.A. Kumar, A.K. Kanjarla, S.R. Niezgoda, R.A. Lebensohn, C.N. Tome, Numerical study of the stress state of a deformation twin in magnesium, Acta Mater 84 (2015) 349–358.
[52] C.D. Barrett, H. El Kadiri, M.A. Tschopp, Breakdown of the Schmid law in homogeneous and heterogeneous nucleation events of slip and twinning in magnesium, J. Mech. Phys. Solids 60 (12) (2012) 2084–2099.

[53] M.R. Barnett, Z. Keshavarz, A.G. Beer, X. Ma, Non-Schmid behaviour during secondary twinning in a polycrystalline magnesium alloy, Acta Mater 56 (1) (2008) 5–15.

[54] C. Guo, R. Xin, C. Ding, B. Song, Q. Liu, Understanding of variant selection and twin patterns in compressed Mg alloy sheets via combined analysis of Schmid factor and strain compatibility factor, Mater. Sci. Eng., A 609 (2014) 92–101.

[55] Z.Z. Shi, Y. Zhang, F. Wagner, P.A. Juan, S. Berbenni, L. Capolungo, J.S. Lecomte, T. Richeton, On the selection of extension twin variants with low Schmid factors in a deformed Mg alloy, Acta Mater 83 (2015) 17–28.